Genesis of a Confined X6.4 Flare in a Quadrupolar Magnetic Configuration

Chunming Zhu, Joel Dahlin, C. R. DeVore, Jiong Qiu, Maria D. Kazachenko, V. M. Uritsky

The Astrophysical Journal, 992:139 (12pp), 2025 October 10 https://doi.org/10.3847/1538-4357/ae0297

Genesis of a Confined X6.4 Flare in a Quadrupolar Magnetic Configuration

Chunming Zhu[1], Joel T. Dahlin[2,3], C. Richard DeVore[2,4], Jiong Qiu[1], Maria D. Kazachenko[5,6], and Vadim M. Uritsky[2,7]

[1] Physics Department, Montana State University, Bozeman, MT 59717-3840, USA
[2] Heliophysics Science Division, NASA Goddard Space Flight Center, 8800 Greenbelt Road, Greenbelt, MD 20771, USA
[3] Department of Astronomy, University of Maryland, 4296 Stadium Drive, College Park, MD 20742, USA
[4] Retired Independent Consultant
[5] Department of Astrophysical and Planetary Sciences, University of Colorado Boulder, 2000 Colorado Avenue, Boulder, CO 80305, USA
[6] National Solar Observatory, 3665 Discovery Drive, Boulder, CO 80303, USA
[7] Catholic University of America, 620 Michigan Avenue N.E., Washington, DC 20064, USA
Received 2025 April 11; revised 2025 August 5; accepted 2025 August 25; published 2025 October 9

Abstract

Both eruptive and confined flares—those having and lacking, respectively, an associated large-scale coronal mass ejection—are frequently observed in solar active regions (ARs). The physical mechanisms controlling the nature of these flares are poorly understood, requiring a detailed investigation of both the magnetic environment and the dynamic flare production process within the source region. Here we study a confined X6.4 flare with a failed filament eruption in AR 13590, observed by the SDO spacecraft on 2024 February 22. AR 13590 exhibited a quadrupolar magnetic configuration consisting of one central and two side arcades of low-lying loops, overlain by a fourth arcade of high-lying loops. A potential-field extrapolation contains a low-altitude null point at a height of approximately 5 Mm. This is a classic magnetic-breakout topology, except that the rising filament lay under one of the side arcades. The confined flare generated four ribbons located in all four of the major polarities, and proceeded in two phases, characterized by two successive stages of ribbon brightenings accompanied by forward and then reverse motion of the brightenings along the interior ribbons. We propose that the two phases represent breakout reconnection in the null region, which removed the flux ahead of the rising filament, followed by "anti-breakout" reconnection, corresponding to a reversed process as those flux systems evolved back toward the pre-eruption configuration. We discuss the implications of these observations for understanding how intense flares can occur without the expulsion of material from the solar corona.

Unified Astronomy Thesaurus concepts: Solar flares (1496); Solar extreme ultraviolet emission (1493); Solar corona (1483)

Materials only available in the online version of record: animations

1. Introduction

Solar flares, observed as sudden brightening across a wide range of the electromagnetic spectrum, are believed to result from the rapid release of a large amount of magnetic energy (10^{32} erg) stored in the solar corona (see reviews by A. O. Benz 2008 and L. Fletcher et al. 2011). During a flare, new magnetic loops are generated through magnetic reconnection and shrink toward the Sun, forming a flaring arcade. The heated and accelerated particles travel along the coronal loops toward the lower atmosphere, depositing their energy at the loop footpoints, which typically manifest as two evolving ribbons observable in optical and ultraviolet wavelengths (T. Forbes & E. Priest 1984; G. Poletto & R. Kopp 1986; D. Longcope & J. Klimchuk 2015). However, the flare ribbons can sometimes exhibit complex structures, such as circular (S. Masson et al. 2009; H. Wang & C. Liu 2012; X. Sun et al. 2013; Z. Xu et al. 2017; P. K. Mitra et al. 2023) or X-shaped forms (Y. Li et al. 2016; R. Liu et al. 2016; Y. Kawabata et al. 2017), or configurations with more than two ribbons (e.g., D. R. Williams et al. 2005; B. Schmieder et al. 2006; R. Joshi et al. 2022; M. D. Kazachenko et al. 2022; J. Jing et al. 2024). The complex geometry of flare ribbons reflects the three-dimensional multipolar configuration of magnetic reconnection beyond the simple 2.5D bipolar standard model (CSHKP; H. Carmichael 1964; P. A. Sturrock 1966; T. Hirayama 1974; R. A. Kopp & G. W. Pneuman 1976) used to describe eruptive flares.

There are two basic types of solar flares based on whether or not they are associated with coronal mass ejections (CMEs), known as eruptive or confined flares (Z. Svestka 1986). A statistical study by S. Yashiro et al. (2005) suggested that the CME-flare association rate increases with the flare's magnitude measured by the soft X-ray peak flux and that over 90% of X-class flares are eruptive and an even higher association rate for huge flares (above X3 level). Recent studies found that the flare eruptivity is affected by several magnetic properties of the hosting ARs (see the review by M. D. Kazachenko et al. 2022, Section 5.5). First, the degree of nonpotentiality, characterized by magnetic free energy, helicity, twist, etc., is found to be indicative of the ability of the flare to erupt. Second, the magnetic field overlying the to-be-erupted structure, also often referred to as the strapping field: its magnitude and decay rate with height, describe how strongly the overlying field inhibits outward expansion. The competition between these two factors in a given configuration is helpful for understanding the likelihood of a given configuration to host eruptive versus confined flares, and in observations

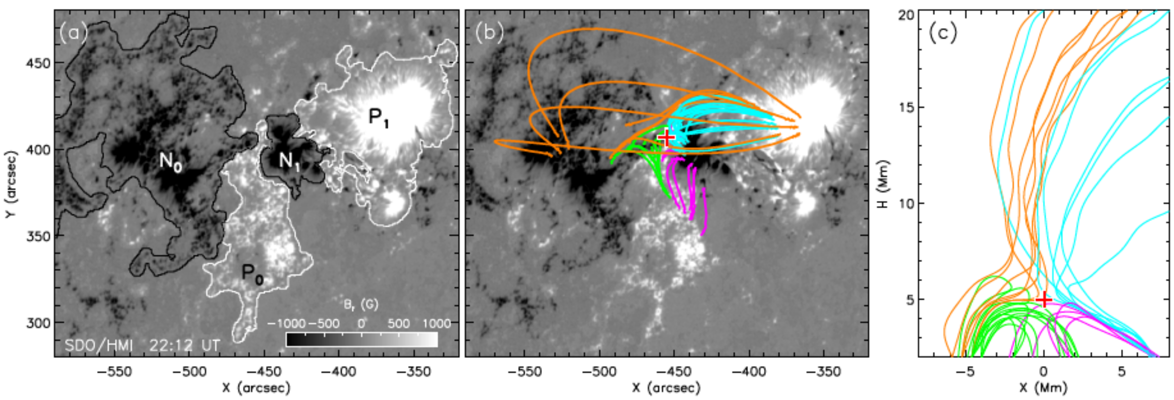

Figure 1. Quadrupolar magnetic configuration of AR 13590. (a) The background (gray color scale) is the normal magnetic field component observed by SDO/HMI during the X6.4 flare on 2024 February 22. The positive/negative polarities are displayed in white/black colors. The boundaries of the four polarities are denoted with contours at around 100 G. (b) Extrapolated magnetic field lines using potential field extrapolation. The location of an existing null point is marked with a red plus sign. Panel (c) showcases the extrapolated loops around the null point viewed from the south.

it is measured in various ways: the total unsigned magnetic flux of the hosting active region (T. Li et al. 2021), the fraction of the active region magnetic flux or area swept by flare ribbons relative to the active region flux or area (S. Toriumi et al. 2017; J. Tschernitz et al. 2018; T. Li et al. 2020; M. D. Kazachenko 2023), and the relative nonpotentiality, or ratio of twist near the polarity inversion line (PIL), where the flare occurs, to the active region magnetic flux (T. Li et al. 2022). Recently, from the largest up-to-date statistical study of thermal and magnetic properties of 480 confined and eruptive flares (GOES class C5.0 and above), M. D. Kazachenko (2023) find that confined flares result from reconnection between more compact, stronger, and lower-lying magnetic fields within larger active regions, which reorganize a smaller fraction of the regions' magnetic flux. This reconnection occurs more rapidly and ends sooner than in the case of eruptive flares. Specifically, for a subset of 216 flares stronger than M1.0 class, the mean peak reconnection rate (unsigned) is $1.9 \times 10^{19}\,\mathrm{Mx\,s^{-1}}$ for confined flares, compared to $1.6 \times 10^{19}\,\mathrm{Mx\,s^{-1}}$ for eruptive flares (see Table 2 in M. D. Kazachenko 2023).

Due to the high CME-flare association rate for large flares, confined flares are relatively rare in solar eruptions exceeding the X3 level. J. Feynman & A. J. Hundhausen (1994) reported no CME associated with an X4.0 flare on 1989 March 9th, highlighting that the absence of a CME in such strongest flares has important implications for understanding CME mechanism. In the past decade, vector magnetic field measurements with high resolution have been available, and several studies have been conducted to explore the detailed magnetic properties of large confined flares. For example, X. Sun et al. (2015) compared a confined X3.1 flare from AR 12192 with two eruptive X-class flares from different active regions. They found that although the area, flux, and magnetic energy of AR 12192 were much larger than for the other two active regions, it exhibited weaker nonpotentiality and had a stronger overlying field, providing a plausible explanation for its failure to produce CMEs.

The rarity of such events makes it challenging to generalize what factors may be involved in the confinement of X-flares. In this article, we present a case study of a confined X6.4 flare from 2024 February 22, which was among the strongest confined flares ever recorded. We argue that the confinement of this flare is best understood in terms of dynamic reconnection at a low-lying coronal null within a multipolar configuration where the magnetic fluxes of the outer polarities dominated those of the inner polarities. In Section 2, we present detailed observations of a failed eruption of a filament and unusual flare evolution, involving a reversal of the ribbon propagation. We present a schematic interpretation of these results, supported by idealized MHD modeling, in Section 3. We conclude with a summary and discussion in Section 4.

2. Observations

On 2024 February 22, an X6.4 flare (SOL2024-02-22T22:08:00) was recorded by the Geostationary Operational Environmental Satellite (GOES) spacecraft, representing one of the strongest flares in solar cycle 25. Here we focus on the SDO observations to study the generation and evolution of this intensive flare. The Atmospheric Imaging Assembly (SDO/AIA; J. R. Lemen et al. 2012) onboard SDO provides full-disk images of the Sun in 10 EUV/ UV channels ($\log T$[K] 3.7–7.3) at a pixel size of 0.″6, and a cadence of 12 s in EUV and 24 s in UV wavelengths. SDO's Helioseismic and Magnetic Imager (SDO/HMI; P. H. Scherrer et al. 2012) takes full-disk magnetograms with 1 spatial resolution at 45 s cadence.

The source region hosting this X6.4 flare is AR 13590, which features a complex quadrupolar magnetic configuration (see Figure 1(a), the boundaries of the four polarities are marked with contours at 100 G). The outer two polarities (N_0 and P_1) cover larger areas than the inner two (P_0 and N_1). The areas of the four polarities (N_0, P_0, N_1, and P_1) are $[106, 24, 8, 41] \times 10^{18}\,\mathrm{cm^2}$. The total magnetic fluxes in the four polarities are $[-25.9, 6.3, -3.9, 23.5] \times 10^{21}$ Mx, respectively. The significant ratio (4–6) of the magnetic fluxes between the outer and inner polarities suggests the presence of dominant overlying fields connecting the N_0 and P_1 polarities.

To help reveal the magnetic configuration of the source region, we generated the potential field extrapolation with a Green's function method (J. J. Aly 1989), as shown in Figure 1(b). The extrapolated field lines connecting various polarities are represented in distinct colors. Furthermore, the extrapolation indicates the presence of a low-lying null point (e.g., E. R. Priest & V. S. Titov 1996; C. J. Schrijver & A. M. Title 2002; D. W. Longcope & C. E. Parnell 2009) with an approximate height of 5 Mm, as marked by a red plus sign in Figures 1(b) and (c). This location was quantitatively determined using the iterative Newton–Raphson method (A. L. Haynes & C. E. Parnell 2007).

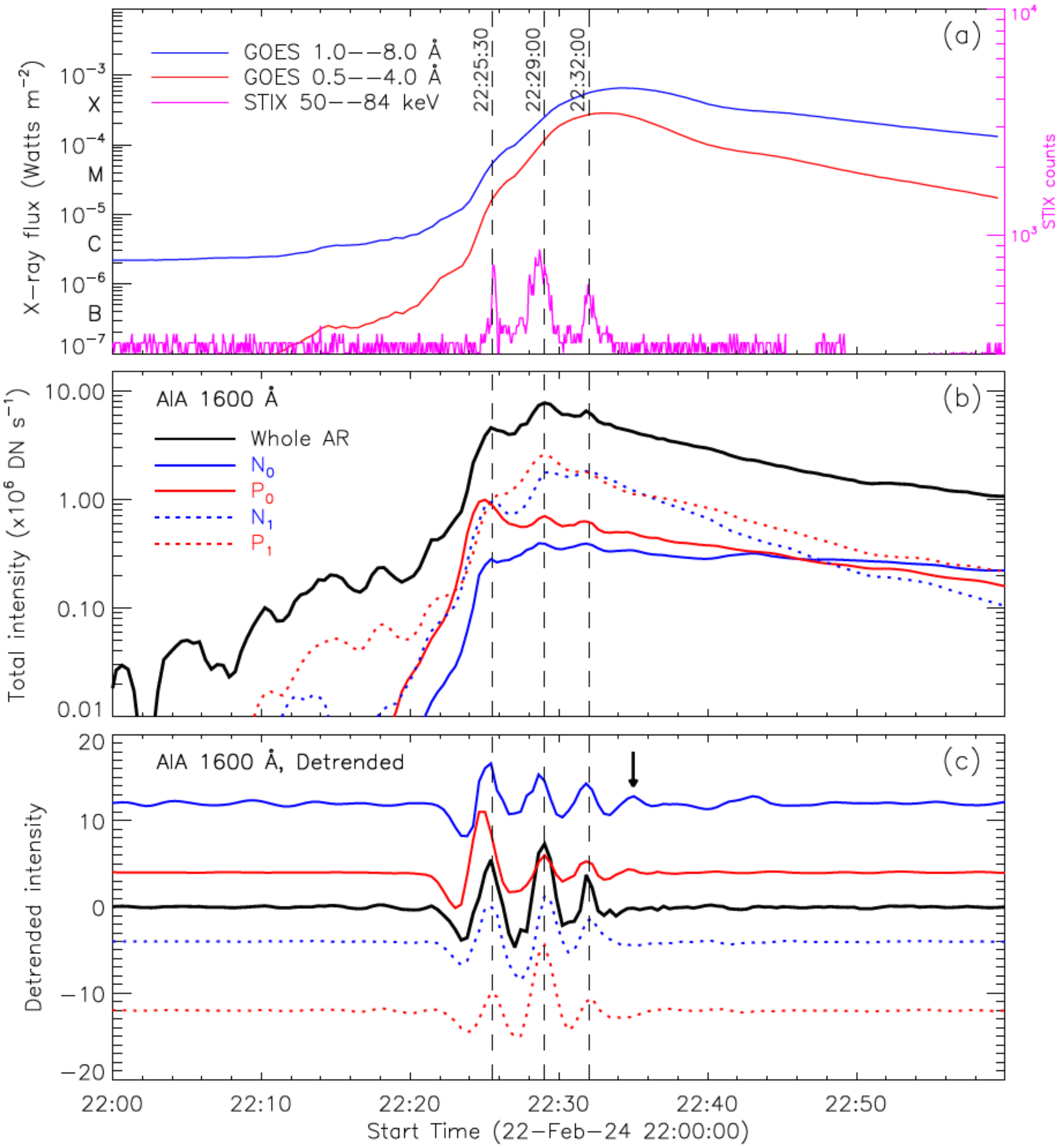

Figure 2. Lightcurves of the X6.4 flare. (a) GOES X-ray fluxes in the low and high channels. STIX 50–84 keV lightcurve (shifted to Earth time) is displayed in magenta color. (b) Total AIA 1600 Å intensities of the whole AR (black) and those in the four polarities as described in the legend. The three dashed lines denote local peaks in AIA 1600 Å and STIX 50–84 keV. (c) Similar to (b), but showing detrended intensities of AIA 1600 Å. The profiles in each polarity are shifted up/down to avoid overlapping. Images of the ribbon evolution in AIA 1600 Å are displayed as an animation, with the boundaries of the four polarities outlined by contours. The animated images run from 2024 February 22 22:10 to 22:53 UT, with a real-time duration of 5 s.

(An animation of this figure is available in the online article.)

This X6.4 flare began at 22:08 UT, peaked at 22:34 UT, and ended at 22:42 UT (Figure 2(a)). The Quicklook (QL) lightcurve in the energy range of 50–84 keV from the Spectrometer/Telescope for Imaging X-rays (STIX; S. Krucker et al. 2020) on Solar Orbiter displays three spikes (marked by vertical dotted lines), suggesting a multiple-step energy release process in this intense flare.

We integrate the flare ribbon emission as observed in SDO/AIA 1600 Å (with a significant contribution by C IV line during flares, see P. J. A. Simões et al. 2019) in the whole AR and the four polarities, respectively, see Figure 2(b). All these lightcurves also display the three peaks at almost the same time as in the hard X-rays. This suggests that the multiple-step energy release processes involve the whole magnetic system rather than localized behavior.

The detrended lightcurves, obtained by subtracting the smoothed curves with a boxcar lasting 5 minutes, are shown in Figure 2(c). All four polarities exhibit multiple simultaneous spikes, which display oscillatory behavior. This oscillatory behavior is consistent with the recently reported quasiperiodic pulsations covering the whole AR observed in this X6.4 flare (D. Li et al. 2024). One difference is that the curves from the eastern two polarities of N_0 and P_0 exhibit a 4th spike (indicated by an arrow) with continuous damping, which was

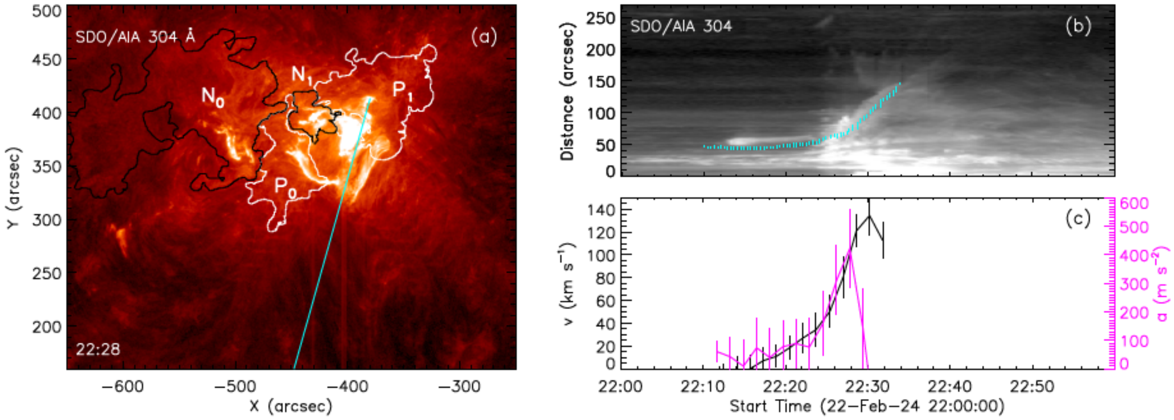

Figure 3. A failed filament eruption between the western two polarities of N_1 and P_1. (a) Snapshot of the eruption observed by SDO/AIA 304 Å at 22:28 UT. The contours of the four polarities are the same as in Figure 1(a). A virtual slit (solid line) tracks the filament eruption. (b) Spacetime stack plot along the virtual slit. The projected filament height is marked with short bars. (c) The corresponding velocity (in black) and acceleration (in magenta) profiles of the filament. An animation of this failed filament eruption in AIA 304 Å (panel (a)) spans from 2024 February 22 22:05 to 22:40 UT, with a real-time duration of 4 s. The animated images are annotated with a solid line for the virtual slit, but the contours of the four polarities are not shown.

(An animation of this figure is available in the online article.)

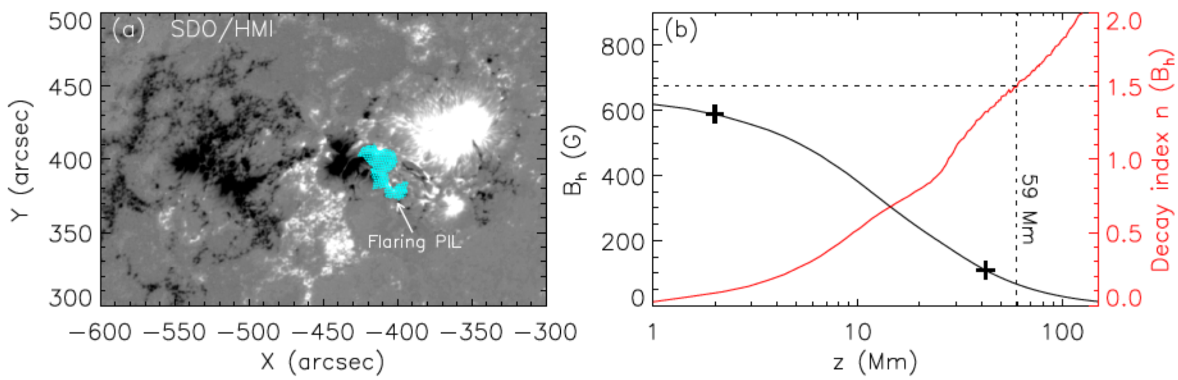

Figure 4. Decay index above the PIL near the flare ribbons beside the filament. (a) The flaring PIL is associated with the filament, shown in cyan color, using the same method from X. Sun et al. (2015). (b) Profiles of overlying field strength B_h (in black) and decay index n (in red) above this flaring PIL region, using the median values along the PIL at varying heights from potential field extrapolation. Two heights at 2 Mm and 42 Mm are marked with plus signs. A vertical dotted line marks the critical height ($n = 1.5$) of 59 Mm.

not reported in D. Li et al. (2024). This 4th spike is not detected in the same profiles of N_1 and P_1, possibly buried by much stronger total intensities (around 3 times larger) in both polarities at that time.

2.1. Failed Eruption of a Filament

A short filament (65 Mm), with its northern/southern footpoints anchored at N_1/P_1. When viewed from the positive polarity side (P_1), the magnetic field along the filament is toward the right, thus it has a dextral chirality (S. F. Martin et al. 1994; S. F. Martin 1998). The filament began to rise around 22:15 UT and subsequently moved toward the southeast, making it a nonradial motion (N. Gopalswamy et al. 2000; P. Liewer et al. 2015), see Figure 3 and the associated animation in AIA 304 Å. A virtual slit along the direction of eruption (Figure 3(a)) is chosen to generate a time-space stack plot (Figure 3(b)). The trajectory of the eruption is tracked by short bars, whose widths denote the error estimate. The corresponding time derivatives give the velocity and acceleration profiles as in Figure 3(c). The projected velocity peaks at 22:30 UT with 134   17 km s^{-1}. The projected acceleration peaks at 22:28 UT with 422   138 m s^{-2}. According to the CME catalogs including Solar Terrestrial Relations Observatory (STEREO) COR1 CME catalog[8] and the catalog compiled using the Computer Aided CME Tracking software (CACTus; E. Robbrecht & D. Berghmans 2004; E. Robbrecht et al. 2009), no CME was reported to be associated with this event, suggesting this X6.4 flare is confined.

To study the confinement of the overlying fields to the filament, we utilized the potential field extrapolation and evaluated the decay index (B. Kliem & T. Török 2006) above the filament, $n = -\partial \ln B_h / \partial \ln z$, indicating how fast the horizontal field B_h decreases with height z. Using the same method from X. Sun et al. (2015), we identified the flaring PIL by combing the dilated regions of the PIL and flare ribbons near the filament, as seen in Figure 4(a).

Figure 4(b) illustrates the variation of the field strength B_h with height (in black) and the decay index n (in red) above the flaring PIL region. The median values of B_h gradually decrease from 630 G near the solar surface to 28 G at a height of 100 Mm. The torus instability is expected when n reaches a critical threshold (e.g., B. Kliem & T. Török 2006). In this event, the critical height (at $n = 1.5$) is 59 Mm, as indicated by the horizontal dotted line in Figure 4. Additionally, the ratio B_h

[8] https://cor1.gsfc.nasa.gov/catalog/

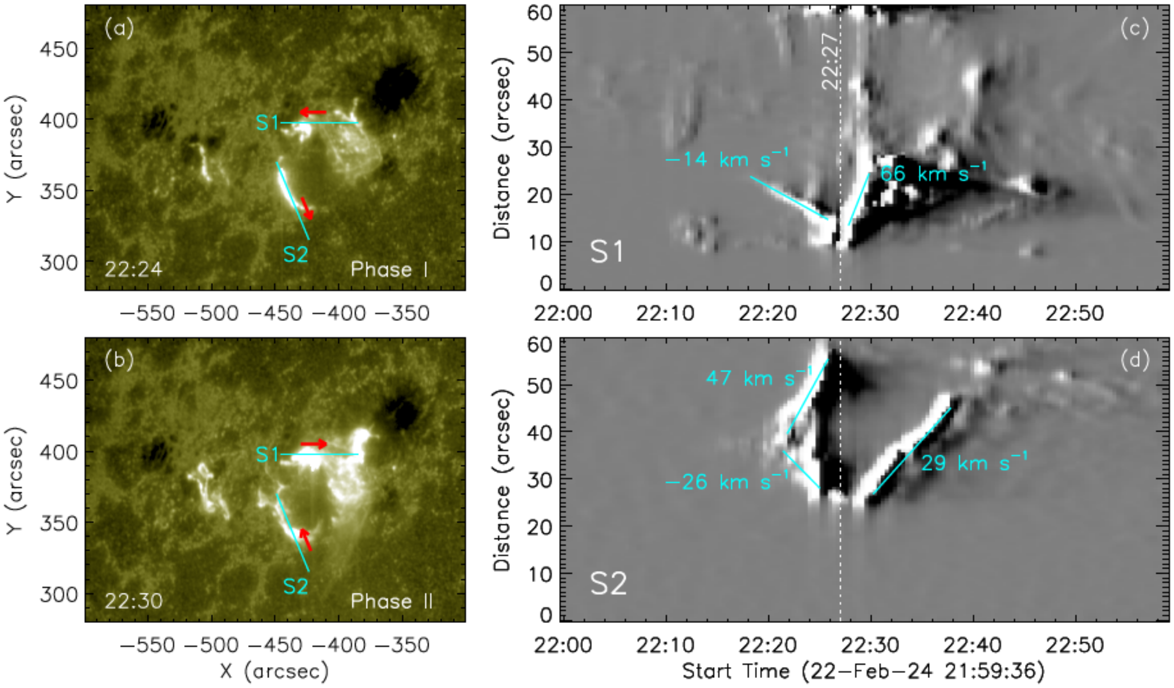

Figure 5. Reverse motions of the two ribbons at the two inner polarities. (a, b) AIA 1600 Å observations of the flare ribbons before and after 22:27 UT when the reverse motion started. Two virtual slits are denoted by the solid lines with the start points at S1 and S2. The reversal of the ribbon propagation along each slit are marked with the red arrows. (c, d) Running difference spacetime stack plots along S1 and S2, respectively. Linear fittings to the trajectories are marked, giving the corresponding velocities. An animation displays the propagation of the ribbons (panels (a), (b)), with two virtual slits overlaid. It runs from 2024 February 22 21:30 to 22:30 UT and has a real-time duration of 14 s.

(An animation of this figure is available in the online article.)

at 42 Mm (typical initial height of erupted filaments, see Y. Liu 2008) to B_h at 2 Mm, $B_h(42)/B_h(2)$, is 0.2. Both values fall between those reported for major confined and eruptive flares reported in X. Sun et al. (2015; see their Table 1), suggesting that this flare might be marginally confined.

2.2. *Reverse Motions of Flare Ribbons*

The inner two flare ribbons at polarities of P_0 and N_1, as observed from AIA 1600 Å, display forward and then backward motions (see Figure 5 and the associated animation). We selected two virtual slits, S1 and S2, as shown in Figures 5(a), (b). The corresponding spacetime stack plots are given in panels (c) and (d). The start points of the virtual slits are labeled with "S1" and "S2," respectively. The ribbon propagation velocities have been estimated by analyzing the slopes of the expanding bright features in these stack plots.

For the ribbon motion along S1, a brightening appeared at 22:20 UT and moved sequentially toward the east until 22:27 UT, with an average velocity of 14 km s^{-1}. Subsequently, the ribbon motion reversed, moving westward at 66 km s^{-1}. Similarly, the motion along S2, which also began around 22:20 UT, with the ribbon expanding simultaneously toward the north and south at velocities of 47 km s^{-1} and 26 km s^{-1}, respectively. The southern motion also reversed at 22:27 UT and moved north at 29 km s^{-1} until 22:40 UT.

2.3. *Flare Evolution in Two Phases*

The reversal motion of the flare ribbons at 22:27 UT naturally separates the flare evolution into two phases (Phases I and II), which precede and follow the reversal motion, respectively. In addition to the ribbon propagation, the two distinct phases are also clear in the ribbon lightcurves and the reconnection rate profile, which we examine, respectively, in Sections 2.4 and 2.5. Here we present the detailed flare development in the two phases.

During Phase I (upper panels of Figure 6), as the filament (thick magenta curve in Figure 6(a)) rises toward the southeast, some newly formed loops (red curves) were observed in AIA 131 Å (10 MK). These new and hot loops connect the polarities of N_1–P_1, N_1–P_0, and N_0–P_1, respectively. Meanwhile, there were some cusp-shaped flare loops (marked with an arrow) extending to the east, between the overlying loops (N_0–P_1) and lower loops (P_0–N_1). The location of the cusp-shaped loops agrees well with the null point (marked with a plus sign, same as in Figure 1(b)). The modest 10 displacement between the two is reasonable given the limitations of potential field extrapolations for modeling the complex magnetic field of active regions.

The newly formed overlying and lower loops may result from the magnetic fields (N_1–P_1) directly above the rising filament interacting with those loops connecting N_0–P_0 near the null point, removing flux ahead of the rising filament, i.e., the breakout process (S. K. Antiochos et al. 1999; P. F. Wyper et al. 2017). The arcade of new loops N_1–P_1 can be expected to result from the tether-cutting process (R. L. Moore et al. 2001) due to the stretch of the rising filament.

Beginning at around 22:25 UT, some long loops connecting N_0 and P_1 (dashed curve in Figure 6(b)) brightened in AIA 131 Å, with their western footpoint coinciding with that of the filament. The filament then underwent an untwisting motion (see animations associated with Figures 3 and 6 during 22:25–22:29 UT). This motion can be tracked using a filament strand in panel (c), which is generated along slit S3 marked in

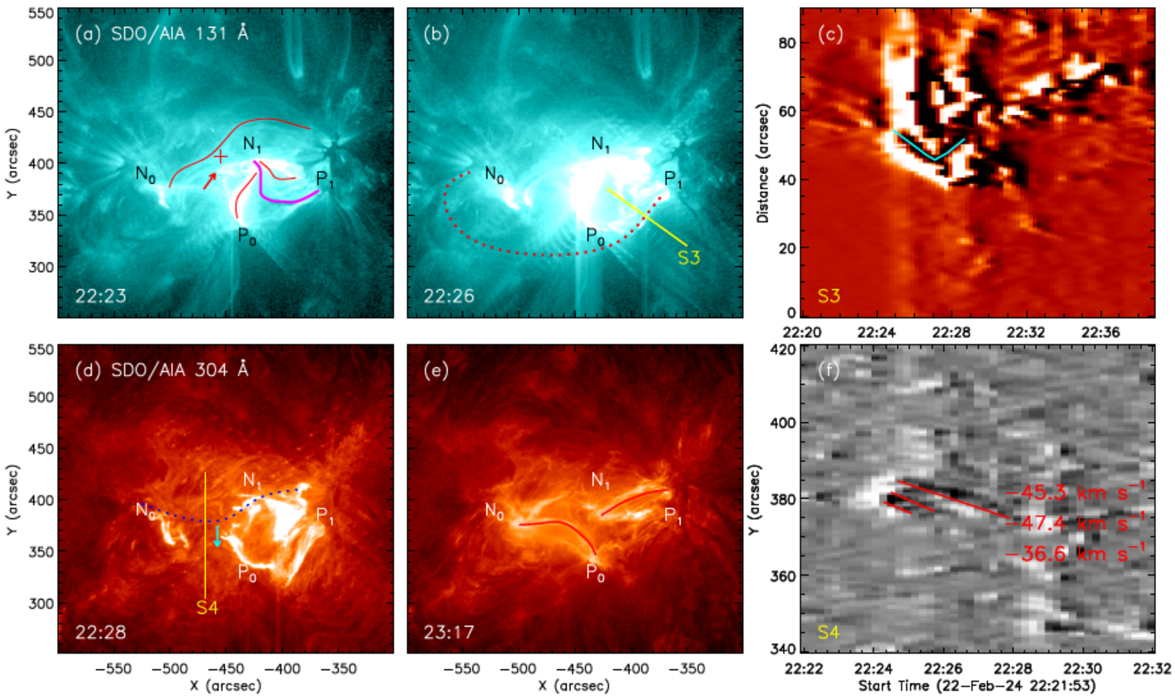

Figure 6. The eruption process of the X6.4 flare. (a) The location of the filament is marked with a thick magenta curve, at the beginning of the flare observed in AIA 131 Å. Newly formed flare loops in Phase I are marked with red curves. The null point location is marked with a red plus sign, same as in Figure 1(b). (b) The filament changes its northern foot to the remote polarity N_0, with the new loops marked with the dotted curve. (c) The untwisting motion of a strand of the filament along slit S3 in panel (b). (d) Long overlying loops display projected motion toward the south. (e) Newly formed loops in Phase II were observed in AIA 304 Å, connecting the side polarities between N_0–P_0 and N_1–P_1, respectively. (f) Running difference spacetime stack plot showing motions of the overlying fields along slit S4 in panel (d). An animation showcases the evolution of the flare loops in AIA 131 Å (panels (a), (b)). It runs from 2024 February 22 21:30 to 23:30 UT, with a real-time duration of 15 s.

(An animation of this figure is available in the online article.)

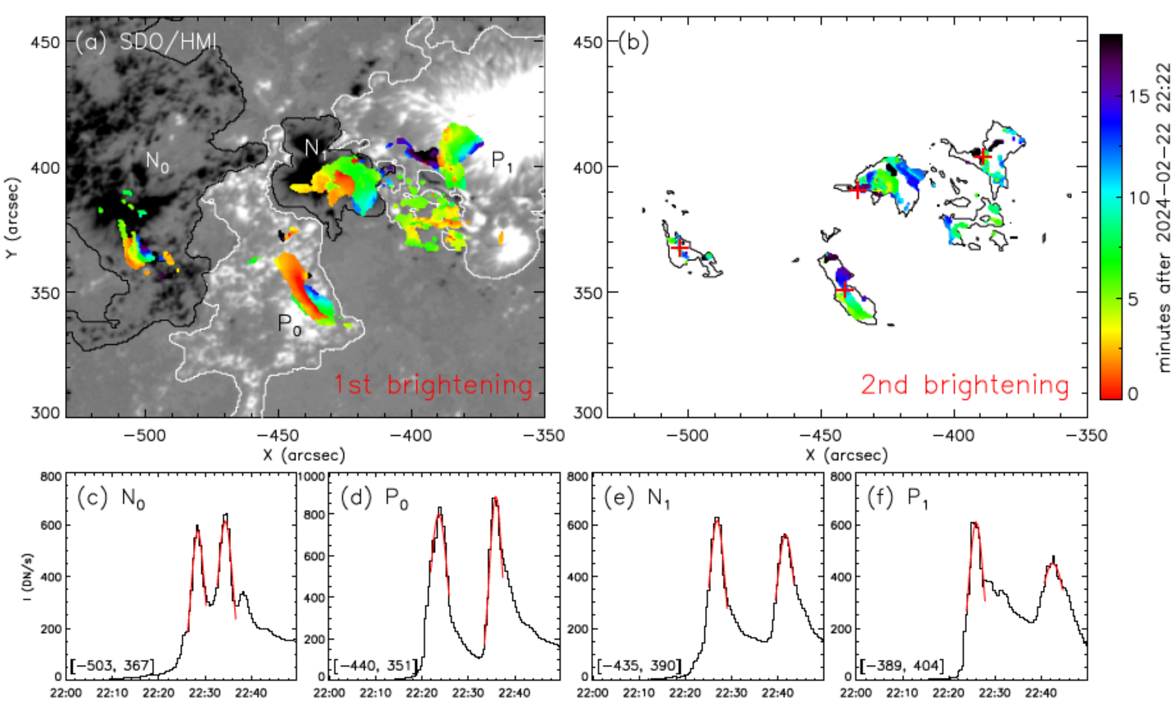

Figure 7. Evolution of the ribbons in the four magnetic polarities. (a) First brightening of the ribbons. The start time of each pixel's first brightening is denoted by the color as shown in the color bar on the right. (b) Some locations of the ribbon display a second brightening. The contours mark the boundaries of the ribbons in (a). The same color bar in (a) is used to denote the start time of the second brightening. (c)–(f) AIA 1600 Å lightcurves of selected flaring pixels with one in each polarity, are marked with red "+" signs in panel (b). Their coordinates (in arcsec) are noted at the lower left of each panel. The red curves are Gaussian fittings to each local peak.

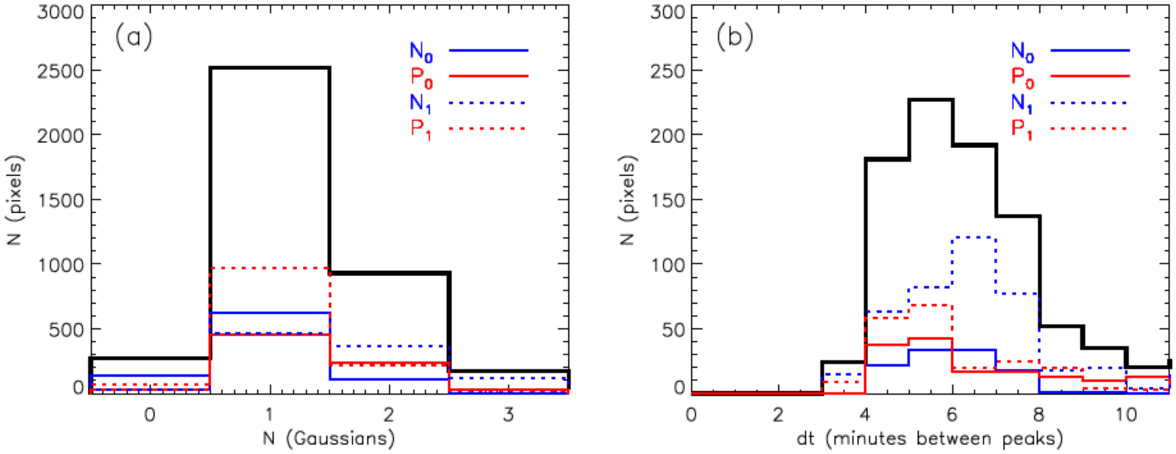

Figure 8. Statistics of the ribbon brightening. (a) Number of pixels for the number of Gaussian components identified at each flaring pixel. (b) Distribution of the time difference between the two peaks at the pixels with multiple brightening. The black curve is for the whole flare region, while the colored curves correspond to the four polarities.

panel (b). The untwisting ends at around 22:29 UT, and thus lasts for about 4 minutes. The filament material shot along the new loops (N_0–P_1), and then most fell back to the P_1 region starting from 22:44 UT. These observations suggest that the filament switched its northern footpoint from N_1 to N_0 during this process.

Meanwhile, some overlying loops (N_0–P_1) were observed moving southward starting at 22:25 UT, with the direction indicated by an arrow in Figure 6(d). Some of these loops disappeared as early as 22:27 UT, while most vanished around 22:31 UT when they arrived approximately above the region of the inner loops P_0–N_1. The motion of these loops was tracked with a running difference spacetime stack plot along a virtual slit, "S4," with the results shown in Figure 6(f). These loops had a projected velocity of 43.1 5.7 km s^{-1}. At the end of this flare, some newly formed flare arcades connecting the outer polarities (N_0–P_0, N_1–P_1) were observed, as displayed in Figure 6(e). Thus, in Phase II, the southward motion and subsequent disappearance of the overlying fields, followed by the formation of flare arcades connecting the outer polarities, suggest ongoing reconnection occurring between the overlying fields and those between the inner two polarities. This scenario corresponds to a reversed process of the breakout reconnection in Phase I, i.e., an "antibreakout" process (P. MacNeice et al. 2004; B. J. Lynch et al. 2008), restoring the pre-eruption magnetic field configuration.

2.4. Recurrent Brightening of the Flare Ribbons

Some locations of the flare ribbons experience two brightenings, for example, where the reverse motion occurs as seen in Figure 5. Here we look into the spatial and temporal characteristics of the flare ribbons. To identify the flare ribbons, we focused on flaring pixels in the AIA 1600 Å passband with intensities greater than 5 times the median preflare intensity of the active region (20 DN s^{-1}) for a duration of at least 3 minutes (J. Qiu et al. 2010). A total of 3945 ribbon pixels were identified. Thus, the total area of the flare ribbons is 9.5×10^{18} cm^2. And the ratio of ribbon-to-AR areas is 5.3%, near the upper limit of the typical range ([2.6%, 6.1%], see Table 2 in M. D. Kazachenko 2023) for confined flares.

The locations of the identified ribbon pixels are displayed in Figure 7(a), with each pixel's color denoting the flaring's start time (see the color bar to the right), which we note as the first brightening. Among these, the intensity profiles of a subset of 1152 (29%) pixels exhibited additional peaks. Their locations and start times of the second brightening are shown in Figure 7(b), where the contours mark the boundaries of the first brightenings in panel (a). The lower panels (c)–(f) present the intensity profiles of four selected locations, each from a different polarity and marked by a red plus sign in panel (b). We applied multiple-Gaussian fitting to each profile and identified local peaks with intensities exceeding a threshold of 400 DN s^{-1}. The fitting results near the local peaks are highlighted with red curves over the intensity profiles. These profiles indicate that these pixels experienced two heating pulses separated by a few minutes.

The statistical results of the fitting applied to the flaring pixel lightcurves are shown in Figure 8. Panel (a) presents the distribution of the number of components for each multiple-Gaussian fitting. In total, 2520 out of 3945 (64%) flaring pixels exhibit a single peak, 931 (24%) pixels exhibit double peaks, and 221 (6%) pixels display three peaks. The remaining 273 flaring pixels have peak intensities below the threshold and are not considered here. Similar distributions from the four polarities are represented by colored curves. The ratio of the number of double to single Gaussians in the four polarities is 0.18/0.53/0.79/0.22 for $N_0/P_0/N_1/P_1$, respectively. It suggests that the lightcurves in the outer two polarities (P_1 and N_0) primarily feature single-Gaussian components, while those in the inner two polarities have a larger portion of double-Gaussian components.

The distribution of the time difference, *dt*, between the two peaks of the double-Gaussian components is illustrated in Figure 8(b). Most of this distribution ranges from 4 to 8 minutes, with a peak at 5.5 minutes. Notably, *dt* from the three polarities N_0, P_0, and P_1 also peak at 5.5 minutes. In contrast, N_1 peaks slightly later, at around 6.5 minutes. This delay might be attributed to the process of tether cutting occurring as the filament rises from this region. J. K. Thalmann et al. (2015) previously observed similar rebrightening behavior in an X1.6 confined flare, with a typical delay of approximately 10 minutes between the two peaks. Y. Xu et al. (2023) studied the plasma motions from a rebrightening region in an X1.3 flare, where the time delay is around 5 minutes.

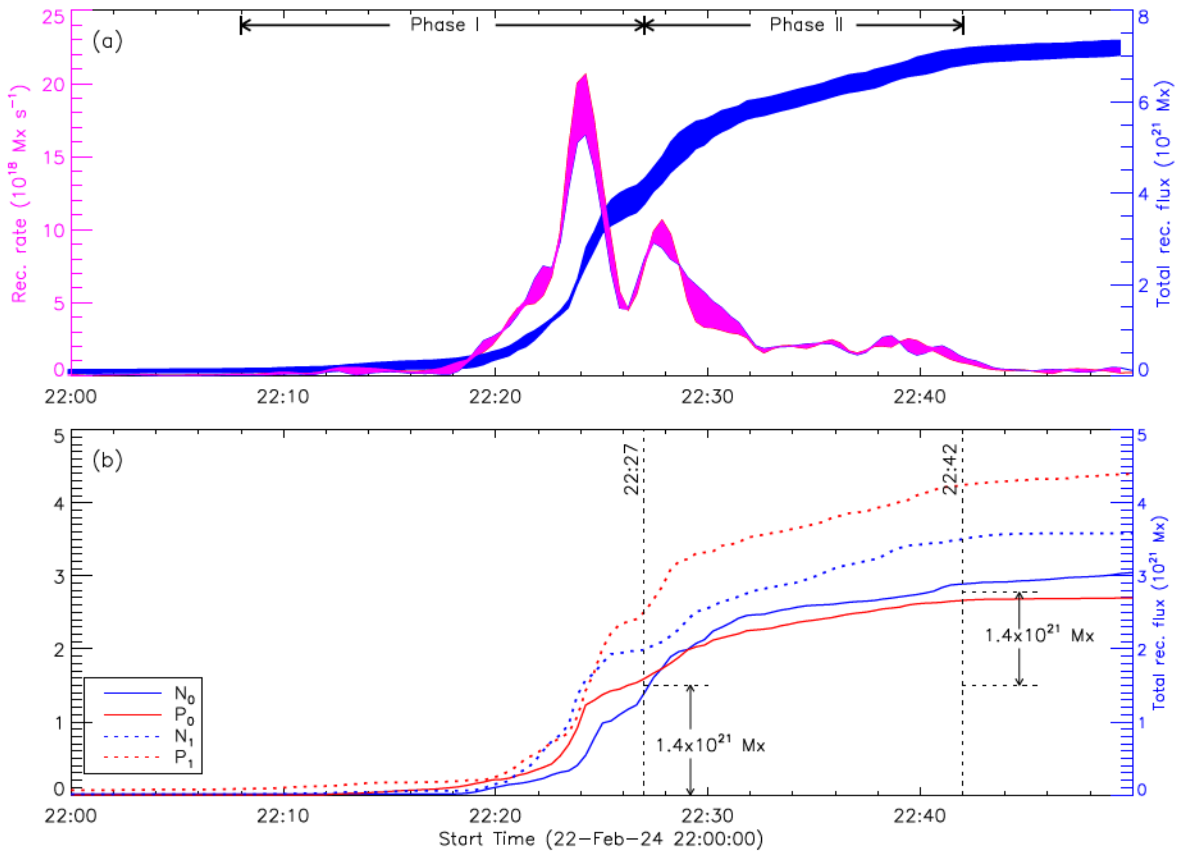

Figure 9. Reconnection rate profiles in this X6.4 flare. (a) The reconnection rate profile is displayed in a pink curve, and the accumulated reconnection flux is in blue. The width of each curve corresponds to the difference of the positive and negative polarities. (b) The total reconnection fluxes for each of the four major magnetic polarities.

How such a delay varies with the magnetic geometry or flare dynamics will be investigated in the future.

2.5. *Reconnection Rate Measurement*

As magnetic reconnection occurs in the corona, the released energy is transferred along the flare loops and deposited at their footpoints, forming the flare ribbons. In this way, the mapping of the reconnection flux in the lower atmosphere has been utilized to measure the reconnection rate by summing up photospheric magnetic fluxes swept through by flare ribbons (e.g., H. Isobe et al. 2002; J. Qiu et al. 2002, 2004; M. D. Kazachenko et al. 2017; C. Zhu et al. 2020). We applied the same method for this X6.4 flare, and the measurements are displayed in Figure 9. It is noted that here we have included the contribution from the second brightening, which accounts for approximately 20% of the total fluxes (Figure 7(b)).

The profiles of the reconnection rate and the accumulated reconnection flux across the entire active region are displayed in Figure 9(a). The reconnection rate profile displays two major peaks of 1.9×10^{19} and 9.7×10^{18} Mx s^{-1}, occurring at 22:24 and 22:28 UT, respectively. The timings of both peaks align closely with the first two peaks in the STIX hard X-ray profile (Figure 2(a)). After that, the rate gradually decreased to the background level by 22:42 UT. The third peak (at 22:32 UT) in the STIX hard X-ray profile is not evident in the reconnection rate profile, likely due to the relatively high threshold (400 DN s^{-1}) used to prioritize the detection of well-defined multiple-peak intensity profiles. The total reconnected flux amounts to 7.3×10^{21} Mx. Both the peak reconnection rate and the total reconnection flux measured in this confined X6.4 flare exceed those of eruptive flare events reported in C. Zhu et al. (2020; see their Table 1). The ratio of the total unsigned magnetic flux within the ribbons to that of the entire AR, R_Φ, is around 24%, aligning with the upper limit of confined events (S. Toriumi et al. 2017; M. D. Kazachenko 2023).

Figure 9(b) illustrates the accumulated reconnection fluxes in the four magnetic polarities individually. The total reconnection fluxes are approximately $3.2/2.7/3.6/4.5 \times 10^{21}$ Mx in the polarities of $N_0/P_0/N_1/P_1$, respectively. Thus, the ratios of reconnection flux to total magnetic flux in each polarity are 12%, 43%, 92%, and 19%. The notably high ratio in polarity N_1 results from extensive ribbon coverage in this polarity (Figure 7(a)) and the contribution related to the second brightening. For the entire AR, the ratio of the ribbon-to-AR magnetic fluxes is 23.4%, close to the the upper limit for confined flares (S. Toriumi et al. 2017; J. Tschernitz et al. 2018; M. D. Kazachenko 2023).

The eastern polarities (N_0 and P_0) have lower reconnection fluxes related to the breakout and antibreakout processes, while the western polarities (N_1 and P_1) have an additional contribution from the tether cutting caused by the filament eruption (Figure 6). The average values of the reconnection fluxes in N_0 and P_0 can thus be used to evaluate the total fluxes added/removed to the overlying fields during Phases I and II (or the breakout/antibreakout processes). During both phases, the average values of the total reconnection fluxes in N_0/P_0 are equal at 1.4×10^{21} Mx (noted in the figure), indicating that the

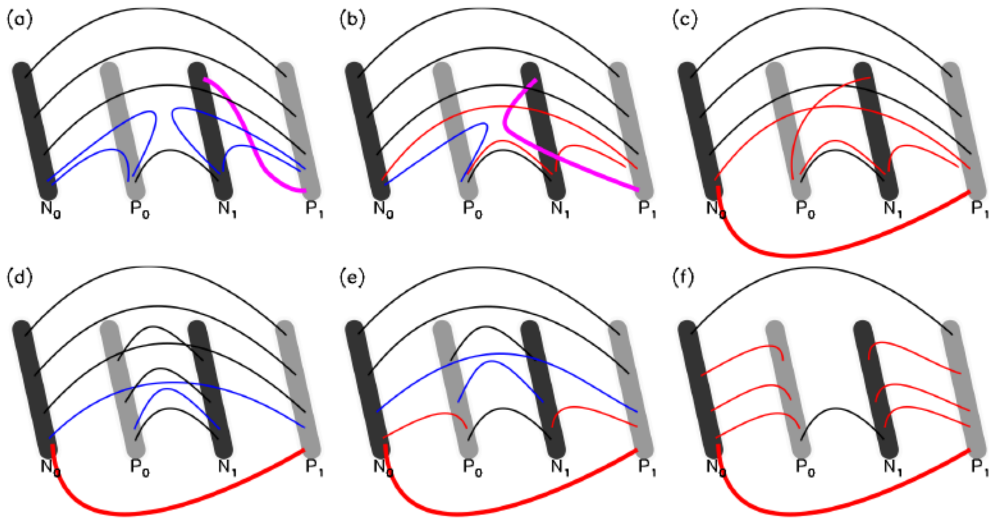

Figure 10. Schematic diagrams for the evolution of the confined X6.4 flare. Top panels: Phase I, breakout reconnection that removes the magnetic flux (blue) ahead of the rising filament (thick magenta), and interaction of the rising filament with its nearby fields. Lower panels: Phase II, antibreakout, relaxation of (overlying) fields progressively reconnecting the short/lower fields toward the north direction.

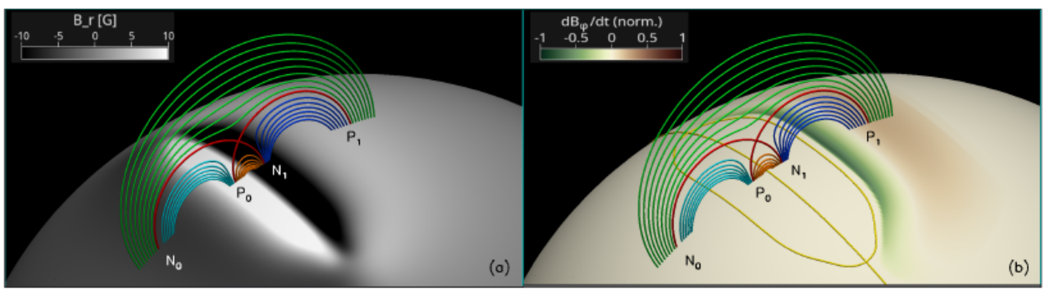

Figure 11. Simulation setup for the numerical model. (a) Initial magnetic field configuration, showing the radial component of the magnetic field (grayscale), four flux systems (green, cyan, blue, orange) and the boundaries between them (red field lines, which meet at the null point). (b) Shearing profile (dB_ϕ/dt, green-brown shading) along the northernmost polarity inversion line (PIL).

amount of flux added to the overlying fields in Phase I might get removed in Phase II.

3. Interpretation

3.1. Schematic Diagrams

We next interpret the flare evolution using the schematic diagrams shown in Figure 10. In each panel, blue curves indicate interacting or reconnecting loops, red curves denote newly formed loops resulting from the reconnection, and black curves represent some surrounding loops. The thick magenta line highlights the filament, while the thick red line represents the newly formed loop containing filament materials.

The quadrupolar configuration (N_0, P_0, N_1, and P_1) is illustrated in Figure 10. The filament is located between the western polarities of N_1 and P_1. As the filament rose, the magnetic fields (N_1–P_1) above it stretched eastward. Near the null point, these fields reconnected with field lines N_0–P_0, in a process known as breakout reconnection. Meanwhile, the fields (N_1–P_1) directly surrounding the filament underwent tether-cutting reconnection. Both of these processes result in the formation of flare loops (marked in red) in Figure 10(b). As the filament continued to rise, it interacted with the eastern loops (N_0–P_0), eventually shifting its northern footprint to N_0 and expanding to the south, as shown by the thick red curve in Figure 10(c).

Subsequently, as shown in Figure 10(d), the overlying fields (N_0–P_1) relaxed and reconnected with the inner field lines (P_0–N_1), creating new loops that linked the outside polarities (N_0–P_0, and N_1–P_1, as shown in panel (e)). This relaxation and reconnection progressively moved northward (Figure 10(e)), forming flaring arcades (N_0–P_0 and N_1–P_1), see panel (f). This step corresponds to the antibreakout process in Phase II.

3.2. Simulation

To interpret the observations described above, we performed a flare simulation with the Adaptively Refined Magnetohydrodynamics Solver (ARMS; C. R. DeVore & S. K. Antiochos 2008), which has been used to great success in modeling many solar eruptive phenomena including extensive investigations of breakout reconnection (e.g., B. J. Lynch et al. 2008, 2009, 2016; J. T. Karpen et al. 2012; S. Masson et al. 2013, 2019; J. T. Dahlin et al. 2019, 2022a, 2022b). To address the essential features of the observations, we employed an idealized initial magnetic configuration adapted from the flare model presented in J. T. Dahlin et al. (2022a), which was characterized by four magnetic polarities (i.e., $-+-+$) that were antisymmetric across the equator. We adjusted the magnetic fluxes of these polarities (parameterized by a series of subsurface dipoles, detailed in the Appendix) so that the flux in the outer polarities was much larger than in the inner

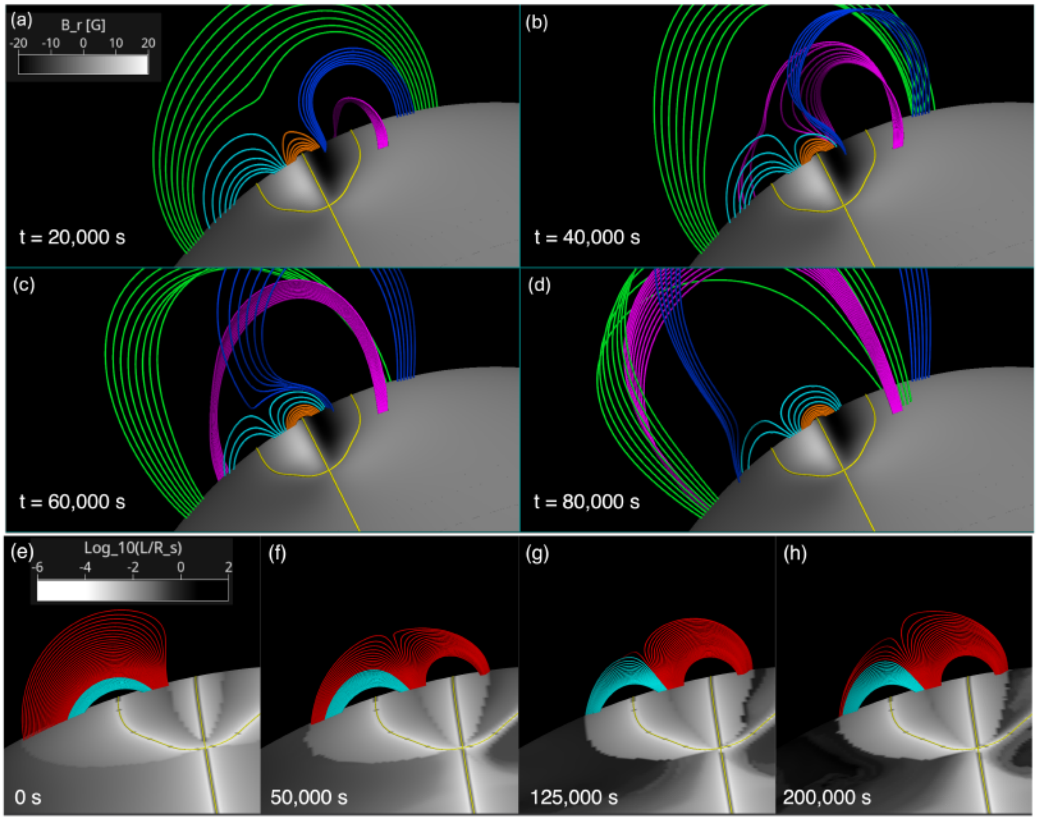

Figure 12. Overview of simulation results. (a)–(d) Buildup of the filament channel (magenta) in response to the shearing at the inner boundary. The other four flux systems are the same as those shown in Figure 11. (e)–(h) Evolution of the "breakout" and "antibreakout" reconnection, as illustrated with two sets of field lines traced from P_0 (center-left polarity). Red (cyan) field lines indicate that do (do not) undergo breakout reconnection during the course of the simulation, as shown for the "high-water" mark of the breakout reconnection at $t = 125{,}000$ (g). The field-line length map (L-map, a term first suggested by M. Kazachenko, e.g., J. T. Dahlin et al. 2019; B. J. Lynch et al. 2019) is shown in grayscale on the solar surface, illustrating the changes in topology in response to the breakout reconnection. An animation of panels (a)–(d), which is the simulation of the buildup of the filament channel, is available. The animation has a real-time duration of 8 s.

(An animation of this figure is available in the online article.)

polarities (>3:1) in order to represent the configuration present in the observations.

To generate a filament channel, we sheared the polarity inversion line between polarities N_1 and P_1 (consistent with the filament located in the observations) using the STITCH method (J. T. Dahlin et al. 2022b). A minimum grid cell size of $\Delta r = 2.66$ Mm and $R_s\Delta\theta = R_s\Delta\phi = 2.16$ Mm at was imposed over the region $R_s < r < 2R_s$; $3\pi/8 < \theta < 5\pi/8$; $-\pi/5 < \phi < \pi/5$ (adaptive refinement was disabled). The initial atmosphere, boundary conditions and domain were identical to those employed in J. T. Dahlin et al. (2022a). The initial magnetic configuration and the shearing profile are shown in Figure 11. The analogs of the observed polarities N_0, P_0, N_1, P_1 stretch from the bottom left to the top right. Shearing is imposed only over the positive polarity region P_1 in order to avoid shearing the central (equatorial) PIL. The propagation of the shear along these short loops occurs over a timescale much shorter than the energy buildup interval, so this choice is reasonable.

The filament channel formation and the resulting breakout reconnection are illustrated in Figure 12. In response to the boundary driving, a highly sheared filament channel forms (magenta field lines in Figure 12(a)). Simultaneously, the overlying loops (green) expand outward in response to the resulting buildup of magnetic pressure due to the buildup of shear (b)–(d). Despite the presence of the coronal null above the filament channel, the magnitude of the overlying flux linking N_0–P_1 (represented by the green field lines) is too great to allow an eruption. Nevertheless, the expansion of the northern arcade (N_1–P_1, blue field lines) pushes the null point southward toward the southern arcade (N_0–P_0, cyan) and triggers breakout reconnection at the null (see especially the "X-point" in Figure 12(c)).

Breakout reconnection at this null point is illustrated in further detail in panels (e)–(g), which show the evolution of field lines traced from P_0 that initially map to N_0 (we show these field lines, rather than those directly overlying the filament channel, because the latter undergo shearing, which makes it difficult to untangle the changes in field-line connectivity that are due to surface motions versus reconnection). The field lines are colorized to highlight the transfer of flux from the southern to the central arcade (the counterpart of the reconnection of the dark blue field lines in panels (c)–(d)), with red indicating those field lines that eventually reconnect, representing a "high-water mark" for the breakout reconnection (panel (g)). In contrast, the cyan field lines retain their connectivity throughout the evolution and do not undergo reconnection.

After t 125,000 s, the dynamics are dominated by "antibreakout" reconnection, which transfers flux from the central arcade back onto the southern arcade (compare panels (g), (h)). This pattern of "breakout" followed by "antibreakout" is consistent with the interpretation of the model described above. The corresponding apparent motion of the footpoints of the breakout current sheet (dark arc separating the cyan and red fluxes at the solar surface in P_0) can then be understood to correspond to the forward and reverse motion of the ribbons in the observations.

We note that the observed magnetic structure is significantly more complex than the idealized simulation employed here. For example, the inner negative polarity region N_1 covers a substantially smaller area than its neighboring positive polarity regions (P_0, P_1). Additionally, there is a region of weak magnetic field at X -400 , Y 350 bounded to either side by the positive polarities (Figure 1(a)). Poor magnetic confinement in this region may explain the nonradial propagation of the failed filament eruption through this region (Figure 3). No similar feature was identified in the numerical model, which is not surprising given the symmetry of the configuration. Regardless, the primary target for the model–data comparison was the reversal of the "breakout" reconnection, which we have successfully verified with the simulation. Importantly, in contrast previous numerical studies that identified antibreakout reconnection, the present simulation modeled flaring/failed eruption from a side arcade in a magnetic environment where the magnetic flux in the outer polarities was much greater than in the inner polarities.

4. Summary

In this study, we present the generation and evolution of an X6.4 flare that occurred on 2024 February 22, which corresponds to one of the most intense confined flares ever observed. The hosting active region, AR 13590, is characterized by a quadrupolar magnetic configuration and features a low-lying null point. A filament situated between the two western polarities erupted nonradially but failed to ascend enough in the higher corona to be identified as a CME. This flare's evolution appears to have two phases, as evidenced by several interesting phenomena: multiple spikes of the chromospheric emissions, the reverse motion of the flare ribbons, changes in the connectivity and motion of the coronal loops, and recurrent brightening of the flare ribbons.

Multiple hard X-ray peaks in solar flares often indicate complex dynamics involved in the generation of these flares (e.g., S. Kim et al. 2007; B. Joshi et al. 2009; Q. Hao et al. 2012; T. Gou et al. 2017; H. Ning et al. 2018; P. Zou et al. 2019; L. Zhang et al. 2024). In the case of this X6.4 flare, a few spikes were detected in the profiles of hard X-ray (Figure 2(a)), AIA 1600 Å (Figures 2(b), (c)), and reconnection rate measurement (Figure 9). The multiwavelength imaging from SDO/AIA, especially the observed motion reversal of the ribbons, suggests that this flare consists of two phases (Figure 10): an initial breakout process followed by the relaxation of overlying fields. A data-inspired simulation further supports this interpretation (Section 3.2).

The strong overlying fields in this intense X6.4 flare likely played a crucial role in confining the filament eruption, preventing it from producing a CME. This scenario is supported in previous studies (e.g., Y. Wang & J. Zhang 2007; Y. Liu 2008; X. Sun et al. 2015). AR 13590 exhibits a quadrupolar configuration, characterized by dominant overlying fields. This is indicated by a significant ratio (4–6) of the magnetic fluxes between the outer and inner polarities. Notably, the filament is situated between the two westernmost polarities, rather than at the center of the active region. In this way, the breakout process during Phase I would enhance the overlying fields (Figures 10(a), (b)), further inhibiting the filament's eruption. Consequently, as a result of the breakout process, the filament and its surrounding magnetic fields became part of the overlying fields connecting the two outer polarities (Figures 10(b), (c)).

It is noteworthy that around 30% of the identified flare ribbon pixels exhibit multiple peaks. A similar phenomenon was reported in another confined X1.6 flare (J. K. Thalmann et al. 2015), suggesting repeated energy release linked to the same magnetic field structures. The ribbon rebrightening can also be expected in the slipping reconnection (e.g., G. Aulanier et al. 2006; J. Dudík et al. 2014) or the drift of the flux rope footpoints (G. Aulanier & J. Dudík 2019; A. Zemanová et al. 2019). However, no clear evidence for the apparent slipping motion of flare loops or footpoint drift is observed in this event. In this X6.4 flare, these recurrent brightening pixels appear to result from the two phases: the breakout process and the relaxation. A future comprehensive survey of the ribbon rebrightening and their motions will help us understand the frequency of such features and their implications for the energy release processes in solar flares.

Acknowledgments

We thank SDO, Solar Orbiter, and GOES for the data support. We also thank the referee for many constructive comments. J.T. D. and C.Z. acknowledge support by NASA Early Career Investigator Program (ECIP) award 80NSSC23K1065. J.Q and C.Z. acknowledge the support of NASA's Heliophysics Guest Investigator program 80NSSC22K0519 and Heliophysics Data Environment Enhancements (HDEE) 80NSSC25K7467. C.R.D., J.T.D., and V.M.U. were supported by NASA's Heliophysics ISFM program at Goddard Space Flight Center. M.D.K. acknowledges support by NASA ECIP award 80NSSC19K0910 and NSF CAREER award SPVKK1RC2MZ3. Resources supporting this work were provided by the NASA High-End Computing (HEC) Program through the NASA Center for Climate Simulation (NCCS) at Goddard Space Flight Center and the Texas Advanced Computing Center (TACC) at The University of Texas at Austin.

Appendix

The initial magnetic field configuration is given by the superposition of 61 magnetic dipoles placed beneath the inner boundary of the simulation. The total magnetic field is given by $\boldsymbol{B}(\boldsymbol{r}) = \sum \boldsymbol{B}_i^{\mathrm{dip}}(\boldsymbol{r})$, where

$$\boldsymbol{B}_i^{\mathrm{dip}} = M_i \left(\frac{R_i^{\mathrm{dip}}}{|\boldsymbol{r} - \boldsymbol{r}_{0,i}|} \right)^3 [3\boldsymbol{n}_i(\boldsymbol{n}_i \cdot \boldsymbol{m}_i) - \boldsymbol{m}_i],$$

$\boldsymbol{n}_i$ is a unit vector in the direction of $\boldsymbol{r} - \boldsymbol{r}_{0,i}$, $\boldsymbol{m}_i$ is the unit vector in the direction of the ith dipole moment, R_i^{dip} is the characteristic length scale, and M_i is the magnitude. The background solar dipole ($i = 0$) is located at $\boldsymbol{r}_{0,0} = [0, 0, 0]$, pointing north ($\boldsymbol{m}_0 = \hat{z}$) with $M_0 = 2$ G and $R_0^{\mathrm{dip}} = R_s$. The active region is comprised of four sets of dipoles oriented in the $\hat{\theta}$ direction.

For $i \in [1, 21]$, $R_i^{\rm dip} = 1.0 \times 10^{10}$ cm, $M_i = 0.6$ G, and

$$r_{0,i} = \left[0.95R_s,\ 0.5\pi,\ 0.12\pi\left(\frac{i-11}{10}\right)\right].$$

For $i \in [22, 30]$, $R_i^{\rm dip} = 2.0 \times 10^{10}$ cm, $M_i = 0.8$ G, and

$$r_{0,i} = \left[0.9R_s,\ 0.5\pi,\ 0.09\pi\left(\frac{i-26}{4}\right)\right].$$

For $i \in [31, 51]$, $R_i^{\rm dip} = 1.0 \times 10^{10}$ cm, $M_i = 1.73$ G, and

$$r_{0,i} = \left[0.886R_s,\ 0.5\pi,\ 0.15\pi\left(\frac{i-41}{10}\right)\right].$$

For $i \in [52, 60]$, $R_i^{\rm dip} = 2.0 \times 10^{10}$ cm, $M_i = 2.30$ G, and

$$r_{0,i} = \left[0.771R_s,\ 0.5\pi,\ 0.1125\pi\left(\frac{i-56}{4}\right)\right].$$

This distribution of dipoles is adapted from J. T. Dahlin et al. (2022a). Our primary change (other than moderate adjustment of the dipole moments) is the addition of a strong large-scale magnetic field ($i \in [31, 60]$) that increases the flux ratio of the outermost polarities (N_0, P_1) with respect to the central polarities (P_0, N_1).

ORCID iDs

Chunming Zhu https://orcid.org/0000-0003-3218-5487
Joel T. Dahlin https://orcid.org/0000-0002-9493-4730
C. Richard DeVore https://orcid.org/0000-0002-4668-591X
Jiong Qiu https://orcid.org/0000-0002-2797-744X
Maria D. Kazachenko https://orcid.org/0000-0001-8975-7605
Vadim M. Uritsky https://orcid.org/0000-0002-5871-6605

References

Aly, J. J. 1989, SoPh, 120, 19
Antiochos, S. K., DeVore, C. R., & Klimchuk, J. A. 1999, ApJ, 510, 485
Aulanier, G., & Dudík, J. 2019, A&A, 621, A72
Aulanier, G., Pariat, E., Démoulin, P., & Devore, C. R. 2006, SoPh, 238, 347
Benz, A. O. 2008, LRSP, 5, 1
Carmichael, H. 1964, A Process for Flares, 50 (Washington, DC: NASA), 451
Dahlin, J. T., Antiochos, S. K., & DeVore, C. R. 2019, ApJ, 879, 96
Dahlin, J. T., Antiochos, S. K., Qiu, J., & DeVore, C. R. 2022a, ApJ, 932, 94
Dahlin, J. T., DeVore, C. R., & Antiochos, S. K. 2022b, ApJ, 941, 79
DeVore, C. R., & Antiochos, S. K. 2008, ApJ, 680, 740
Dudík, J., Janvier, M., Aulanier, G., et al. 2014, ApJ, 784, 144
Feynman, J., & Hundhausen, A. J. 1994, JGRA, 99, 8451
Fletcher, L., Dennis, B. R., Hudson, H. S., et al. 2011, SSRv, 159, 19
Forbes, T., & Priest, E. 1984, SoPh, 94, 315
Gopalswamy, N., Hanaoka, Y., & Hudson, H. 2000, AdSpR, 25, 1851
Gou, T., Veronig, A. M., Dickson, E. C., Hernandez-Perez, A., & Liu, R. 2017, ApJL, 845, L1
Hao, Q., Guo, Y., Dai, Y., et al. 2012, A&A, 544, L17
Haynes, A. L., & Parnell, C. E. 2007, PhPl, 14, 082107
Hirayama, T. 1974, SoPh, 34, 323
Isobe, H., Yokoyama, T., Shimojo, M., et al. 2002, ApJ, 566, 528
Jing, J., Lee, J., Mancuso, M., et al. 2024, ApJ, 972, 110
Joshi, B., Veronig, A., Cho, K. S., et al. 2009, ApJ, 706, 1438
Joshi, R., Mandrini, C. H., Chandra, R., et al. 2022, SoPh, 297, 81
Karpen, J. T., Antiochos, S. K., & DeVore, C. R. 2012, ApJ, 760, 81
Kawabata, Y., Inoue, S., & Shimizu, T. 2017, ApJ, 842, 106
Kazachenko, M. D. 2023, ApJ, 958, 104
Kazachenko, M. D., Albelo-Corchado, M. F., Tamburri, C. A., & Welsch, B. T. 2022, SoPh, 297, 59
Kazachenko, M. D., Lynch, B. J., Welsch, B. T., & Sun, X. 2017, ApJ, 845, 49
Kim, S., Moon, Y.-J., Kim, K.-H., et al. 2007, PASJ, 59, S831
Kliem, B., & Török, T. 2006, PhRvL, 96, 255002
Kopp, R. A., & Pneuman, G. W. 1976, SoPh, 50, 85
Krucker, S., Hurford, G. J., Grimm, O., et al. 2020, A&A, 642, A15
Lemen, J. R., Title, A. M., Akin, D. J., et al. 2012, SoPh, 275, 17
Li, D., Hong, Z., Hou, Z., & Su, Y. 2024, ApJ, 970, 77
Li, T., Chen, A., Hou, Y., et al. 2021, ApJL, 917, L29
Li, T., Hou, Y., Yang, S., et al. 2020, ApJ, 900, 128
Li, T., Sun, X., Hou, Y., et al. 2022, ApJL, 926, L14
Li, Y., Qiu, J., Longcope, D. W., Ding, M. D., & Yang, K. 2016, ApJL, 823, L13
Liewer, P., Panasenco, O., Vourlidas, A., & Colaninno, R. 2015, SoPh, 290, 3343
Liu, R., Chen, J., Wang, Y., & Liu, K. 2016, NatSR, 6, 34021
Liu, Y. 2008, ApJL, 679, L151
Longcope, D., & Klimchuk, J. 2015, ApJ, 813, 131
Longcope, D. W., & Parnell, C. E. 2009, SoPh, 254, 51
Lynch, B. J., Airapetian, V. S., DeVore, C. R., et al. 2019, ApJ, 880, 97
Lynch, B. J., Antiochos, S. K., DeVore, C. R., Luhmann, J. G., & Zurbuchen, T. H. 2008, ApJ, 683, 1192
Lynch, B. J., Antiochos, S. K., Li, Y., Luhmann, J. G., & DeVore, C. R. 2009, ApJ, 697, 1918
Lynch, B. J., Masson, S., Li, Y., et al. 2016, JGRA, 121, 10
MacNeice, P., Antiochos, S. K., Phillips, A., et al. 2004, ApJ, 614, 1028
Martin, S. F. 1998, SoPh, 182, 107
Martin, S. F., Bilimoria, R., & Tracadas, P. W. 1994, in ASIC, Vol. 433, Solar Surface Magnetism, ed. R. J. Rutten & C. J. Schrijver (Dordrecht: Kluwer), 303
Masson, S., Antiochos, S. K., & DeVore, C. R. 2013, ApJ, 771, 82
Masson, S., Antiochos, S. K., & DeVore, C. R. 2019, ApJ, 884, 143
Masson, S., Pariat, E., Aulanier, G., & Schrijver, C. J. 2009, ApJ, 700, 559
Mitra, P. K., Veronig, A. M., & Joshi, B. 2023, A&A, 674, A154
Moore, R. L., Sterling, A. C., Hudson, H. S., & Lemen, J. R. 2001, ApJ, 552, 833
Ning, H., Chen, Y., Wu, Z., et al. 2018, ApJ, 854, 178
Poletto, G., & Kopp, R. 1986, in Proceedings of the Solar Maximum Mission Symposium, Macroscopic electric fields during two-ribbon flares, ed. D. F. Neidig (Sunspot, NM: National Solar Observatory), 453
Priest, E. R., & Titov, V. S. 1996, RSPTA, 354, 2951
Qiu, J., Lee, J., Gary, D. E., & Wang, H. 2002, ApJ, 565, 1335
Qiu, J., Liu, W., Hill, N., & Kazachenko, M. 2010, ApJ, 725, 319
Qiu, J., Wang, H., Cheng, C., & Gary, D. E. 2004, ApJ, 604, 900
Robbrecht, E., & Berghmans, D. 2004, A&A, 425, 1097
Robbrecht, E., Berghmans, D., & Van der Linden, R. A. M. 2009, ApJ, 691, 1222
Scherrer, P. H., Schou, J., Bush, R. I., et al. 2012, SoPh, 275, 207
Schmieder, B., Mandrini, C. H., Démoulin, P., et al. 2006, AdSpR, 37, 1313
Schrijver, C. J., & Title, A. M. 2002, SoPh, 207, 223
Simões, P. J. A., Reid, H. A. S., Milligan, R. O., & Fletcher, L. 2019, ApJ, 870, 114
Sturrock, P. A. 1966, Natur, 211, 695
Sun, X., Bobra, M. G., Hoeksema, J. T., et al. 2015, ApJL, 804, L28
Sun, X., Hoeksema, J. T., Liu, Y., et al. 2013, ApJ, 778, 139
Svestka, Z. 1986, in Proc. of the Solar Maximum Mission Symposium, The lower atmosphere of solar flares, ed. D. F. Neidig & M. E. Machado (Sunspot, NM: National Solar Observatory), 332
Thalmann, J. K., Su, Y., Temmer, M., & Veronig, A. M. 2015, ApJL, 801, L23
Toriumi, S., Schrijver, C. J., Harra, L. K., Hudson, H., & Nagashima, K. 2017, ApJ, 834, 56
Tschernitz, J., Veronig, A. M., Thalmann, J. K., Hinterreiter, J., & Pötzi, W. 2018, ApJ, 853, 41
Wang, H., & Liu, C. 2012, ApJ, 760, 101
Wang, Y., & Zhang, J. 2007, ApJ, 665, 1428
Williams, D. R., Török, T., Démoulin, P., van Driel-Gesztelyi, L., & Kliem, B. 2005, ApJL, 628, L163
Wyper, P. F., Antiochos, S. K., & DeVore, C. R. 2017, Natur, 544, 452
Xu, Y., Kerr, G. S., Polito, V., et al. 2023, ApJ, 958, 67
Xu, Z., Yang, K., Guo, Y., et al. 2017, ApJ, 851, 30
Yashiro, S., Gopalswamy, N., Akiyama, S., Michalek, G., & Howard, R. A. 2005, JGRA, 110, A12S05
Zemanová, A., Dudík, J., Aulanier, G., Thalmann, J. K., & Gömöry, P. 2019, ApJ, 883, 96
Zhang, L., Zheng, R., Xue, Z., et al. 2024, RAA, 24, 045006
Zhu, C., Qiu, J., Liewer, P., et al. 2020, ApJ, 893, 141
Zou, P., Jiang, C., Feng, X., et al. 2019, ApJ, 870, 97